



1 **The SPectrometer for Ice Nuclei (SPIN): An instrument to**  
2 **investigate ice nucleation**

3 **S. Garimella<sup>1</sup>, T. B. Kristensen<sup>2</sup>, K. Ignatius<sup>2</sup>, A. Welti<sup>2</sup>, J. Voigtländer<sup>2</sup>, G. R.**  
4 **Kulkarni<sup>3</sup>, F. Sagan<sup>4</sup>, G. L. Kok<sup>4</sup>, J. Dorsey<sup>5</sup>, L. Nichman<sup>5</sup>, D. Rothenberg<sup>1</sup>, M.**  
5 **Rösch<sup>1</sup>, A. Kirchgäßner<sup>6</sup>, R. Ladkin<sup>6</sup>, H. Wex<sup>2</sup>, T. W. Wilson<sup>7</sup>, L. A. Ladino<sup>8</sup>, J. P. D.**  
6 **Abbatt<sup>8</sup>, O. Stetzer<sup>9</sup>, U. Lohmann<sup>10</sup>, F. Stratmann<sup>2</sup>, and D. J. Cziczo<sup>1</sup>**

7 [1] {Massachusetts Institute of Technology, Cambridge, MA, United States}

8 [2] {Leibniz Institute for Tropospheric Research, Leipzig, Germany}

9 [3] {Pacific Northwest National Laboratory, Richland, WA, United States}

10 [4] {Droplet Measurement Technologies, Boulder, CO, United States}

11 [5] {University of Manchester, Manchester, United Kingdom}

12 [6] {British Antarctic Survey, Cambridge, United Kingdom}

13 [7] {University of Leeds, Leeds, United Kingdom}

14 [8] {University of Toronto, Toronto, Canada}

15 [9] {V-ZUG AG, Zurich, Switzerland}

16 [10] {Swiss Federal Institute of Technology, Zurich, Switzerland}

17 Correspondence to: D. J. Cziczo (djciczo@mit.edu)



1 **Abstract**

2 The SPectrometer for Ice Nuclei (SPIN) is a commercially available ice nuclei counter  
3 manufactured by Droplet Measurement Technologies in Boulder, CO. The SPIN is a continuous  
4 flow diffusion chamber with parallel plate geometry based on the Zurich Ice Nucleation  
5 Chamber and the Portable Ice Nucleation Chamber. This study characterizes and describes the  
6 behavior of the SPIN chamber, reports data from laboratory measurements, and quantifies  
7 uncertainties associated with the measurements. A machine learning approach for analyzing  
8 depolarization data from the SPIN Optical Particle Counter is also presented. Experiments with  
9 ammonium sulfate are used to investigate homogeneous freezing and droplet breakthrough,  
10 experiments with kaolinite, NX illite, and silver iodide are used to investigate heterogeneous ice  
11 nucleation, and results are compared to those from the literature. Overall, we report that the SPIN  
12 is able to reproduce previous CFDC ice nucleation measurements.

13



## 1 **1. Introduction**

2       Aerosol particles are required for the nucleation of cloud droplets and ice crystals in Earth's  
3 atmosphere (Pruppacher and Klett, 1997). Ice nucleating particles (INP) facilitate the formation  
4 of ice crystals via several possible mechanisms, including deposition nucleation, immersion  
5 freezing, and contact freezing (Rogers, 1989; Pruppacher and Klett 1997). Though droplets  
6 freeze homogeneously below temperatures of  $\sim -38^{\circ}\text{C}$ , INP also facilitate freezing below water  
7 saturation at such cold temperatures (Koop et al., 2000). Because of the complexity of the ice  
8 nucleation process, understanding INP interactions with water has been difficult (Boucher et al.,  
9 2013; Stocker et al., 2013). Despite this difficulty, the significant influence that mixed-phase,  
10 and ice clouds have on the Earth's radiative budget and hydrologic cycle makes understanding  
11 the microphysics of cloud formation an important step in quantifying their influence on climate  
12 (Boucher et al., 2013; Stocker et al., 2013).

13       Laboratory measurements allow for the investigation of ice nucleation at specific conditions  
14 with controlled aerosol properties and provide insight into ice formation as it occurs in the  
15 atmosphere. Several types of laboratory instruments have been developed to measure the  
16 efficiency of heterogeneous nucleation of cloud droplets and ice crystals, and many of these  
17 instruments have been deployed to conduct field observations. Among these instruments, the  
18 Continuous Flow Diffusion Chamber (CFDC) (Rogers, 1988) has proven a useful tool to  
19 measure the conditions required to nucleate ice crystals on various INP's. Studies have been  
20 conducted on different nucleation and freezing mechanisms using many types of aerosol particles  
21 under a wide range of temperatures and RH's (Rogers, 1988; Salam et al., 2006; Stetzer et al.,  
22 2008). Improved versions of the original cylindrical chamber described by Rogers (1980) have  
23 been successfully deployed in ground and aircraft based field campaigns (Chen et al., 1998;



1 DeMott et al., 2003a; DeMott et al., 2003b). Development of parallel plate chamber geometry  
2 has simplified several technical aspects of the chamber design (e.g., lower chamber weight, less  
3 complex machining, and simpler refrigeration plumbing than for the cylindrical geometry) at the  
4 expense of edge effects (i.e., deviations from ideality at the chamber edges). One contemporary  
5 parallel plate design is the Zurich Ice Nucleation Chamber (ZINC) (Stetzer et al., 2008), which  
6 has been used for several laboratory studies (e.g., Welts et al., 2009; Welts et al., 2014). The  
7 Portable Ice Nucleation Chamber (PINC), designed as a field-deployable version of the ZINC,  
8 has since been used to conduct several laboratory and field studies (Chou et al., 2011; Chou et  
9 al., 2013; Kanji et al., 2013). In addition, other research groups have also developed similar  
10 chambers (Kanji et al., 2009; Kulkarni et al., 2009; Friedman et al., 2011; Saito et al., 2011).  
11 Adapting the parallel plate design and other features from the ZINC and PINC chambers, the  
12 SPectrometer for Ice Nuclei (SPIN) is a commercially available ice nuclei counter manufactured  
13 by Droplet Measurement Technologies in Boulder, CO. This study characterizes the behavior of  
14 the SPIN chamber and reports data that validate the general design and performance.

15

## 16 **2. Instrument theory and design**

### 17 **2.1 Theoretical principles**

18 CFDC's, such as the SPIN, are used for ice nucleation measurements by exposing aerosol  
19 particles to controlled temperature and relative humidity (RH) conditions. Controlling the  
20 temperature and RH is accomplished by first coating the two parallel plates in the main chamber  
21 and evaporation section with a thin (~1-2 mm) layer of ice. The water vapor partial pressure  
22 directly adjacent to the ice wall is the saturation vapor pressure over ice at the given ice wall  
23 temperature. The two walls are held at different temperatures below 0°C and a laminar air stream



1 flows between the plates. In this idealized configuration, water vapor and heat diffuse from the  
2 warmer to the cooler wall, leading to linear profiles of water vapor partial pressure and  
3 temperature between the two walls. The exponential dependence of saturation vapor pressure on  
4 temperature, according to the Clausius-Clapeyron relation, leads to supersaturated conditions  
5 (with respect to ice) between the two walls, with a maximum close to the position of the aerosol  
6 lamina (Rogers, 1988; Stetzer et al., 2008). Aerosol particles are constrained within this lamina  
7 and surrounded by two sheath flows passed along each wall. This restricts the aerosol to a  
8 narrow range of temperature and supersaturation at which ice nucleation can take place. An  
9 example of the chamber flow and thermodynamic profile is shown in Figure 1.

10 A sufficient temperature gradient between the walls results in the water vapor partial pressure  
11 in the aerosol lamina exceeding the saturation vapor pressure over liquid water. In this case  
12 droplets, in addition to ice, can nucleate on the aerosol particles. Though droplets can be  
13 identified using the SPIN optical particle counter (OPC) (Section 2.2), increasing the size  
14 difference between droplets and ice helps in distinguishing the two phases. To shrink or  
15 eliminate droplets while retaining ice crystals, particles pass through an evaporation section after  
16 the main chamber (Figure 2). The walls in the evaporation section of the chamber are isothermal  
17 and ice coated so the water vapor partial pressure is equal to the saturation vapor pressure over  
18 ice. Droplets are therefore unstable and shrink in a manner akin to the Bergeron-Wegner-  
19 Findeisen process (Rogers, 1988; Pruppacher and Klett 1997). Droplets over a critical size will  
20 not evaporate completely. The main chamber conditions that generate droplets over this critical  
21 size are termed “droplet breakthrough.” These conditions are quantified in experiments described  
22 in Section 4 and represent an upper RH limit for ice nucleation experiments (only) if droplets and  
23 ice crystals are indistinguishable.



## 1 **2.2 SPIN Chamber Design**

2 Figure 3 shows a diagram of the SPIN system, illustrating the refrigeration, air flow control,  
3 and water flow control components. The temperatures of the two chamber walls and the  
4 evaporation section are controlled using compressor-driven refrigeration systems and heater  
5 strips affixed to the walls. The warm wall and evaporation section are cooled using a single-stage  
6 (with R404A refrigerant) refrigeration loop, while the cold wall is cooled using a two-stage (with  
7 R404A first stage refrigerant and R508B second stage refrigerant) refrigeration loop. Ten  
8 solenoid valves (four for the warm wall, four for the cold wall, and two for the evaporation  
9 section) with proportional–integral–derivative (PID) control are used to regulate refrigeration.  
10 Thirty 30W heater strips (twelve on the warm wall, twelve on the cold wall, and six on the  
11 evaporation section) are used to minimize deviations of temperature from the set point by  
12 applying heating via twenty-six independent PID controllers (twelve for each of the warm and  
13 cold walls and two for the evaporation section). Thermocouples that are inserted into the walls  
14 and affixed with thermal epoxy are positioned at sixteen locations on each chamber wall and two  
15 locations on the evaporation section to map variability in temperature (Figure 2). The chamber  
16 itself is machined from aluminum components and junctions are sealed with rubber gaskets.

17 A filtered and dried sheath flow along each wall is circulated through the chamber using a  
18 pump and mass flow controller (MFC). Sample air is drawn into the system by an additional  
19 pump. The incoming sample air is drawn into the sheath flow using a knife-edge inlet similar to  
20 the one used in the ZINC (Stetzer et al., 2008), which splits the sheath into two flows that move  
21 along each wall. The knife-edge also focuses the particle flow to the center of the chamber,  
22 limiting the temperature and supersaturation range experienced by the particles. Figure 2 shows  
23 the dimensions of the main chamber and evaporation section.



1 After passing through the main chamber and evaporation section, the air stream flows  
2 through a linear depolarization OPC that uses four optical detectors for counting, sizing, and  
3 differentiating unactivated aerosol particles, droplets, and ice crystals in the 0.4 - 12  $\mu\text{m}$  size  
4 range. Figure 4 shows the optical diagram of the OPC. The side scatter detector is used for  
5 particle sizing by total scattering intensity, and the backscatter detectors are used to measure P  
6 (parallel to the incident laser light) and S (perpendicular to the incident laser light) polarization  
7 for phase discrimination: ice crystals have been shown to depolarize more light than water  
8 droplets because of their aspherical morphology, and this change in depolarization signal is used  
9 to differentiate the two phases (Liou and Lahore, 1974; Nicolet et al., 2010; Clauss et al., 2013;  
10 Nichman et al., 2015). The OPC laser (Osela ILS-640-250-FTH-1.5MM-100uM) is a continuous  
11 wave 500 mW 670 nm laser with a top-hat beam profile. One of two sets of backscatter optics  
12 has a polarizing beam splitter and measure backscattered light in both P and S polarizations (P1  
13 and S1, respectively). The second set of backscatter optics measures only the P polarization (P2).  
14 The detection angle of both sets of backscatter optics is centered at  $135^\circ$  and has a half angle of  
15  $20^\circ$ .

16 LabView software is used for instrument control and data acquisition. The SPIN software  
17 program consists of several different loops and sub-programs and allows for significant  
18 automation during operation. The Control Program starts and stops the other modules, updates  
19 the displays, controls the instrument set points, watches the alarms, and otherwise supervises the  
20 operation of the entire system. The Data Acquisition Loop acquires data for particle events and  
21 does so in buffers of typically 500,000 to 1,000,000 points in each channel, with 200 to 400 ns  
22 between each data point. This loop acquires data continuously and passes the data buffers to the  
23 Data Processing Loop. The Data Processing Loop examines the data buffers acquired by the



1 Data Acquisition Loop and identifies events within those buffers. It extracts the particle data,  
2 saves them to disk, and supplies them to the Control Program for display. If data loads are high  
3 and the CPU cannot keep up with this processing, some buffers from the Data Acquisition Loop  
4 will be ignored and the duty cycle of the acquisition will drop to less than 100%: for 1 Lpm  
5 sample flow, this corresponds to particle counts higher than ~3900 per cc.

6 User control of the various SPIN components, including the compressors, valves, and  
7 detector is also performed and automated through the LabView interface. Individual actions,  
8 such as toggling valves, as well as sequences, such as icing the chamber walls, are controllable  
9 through software. The software also includes functionality to create custom sequences, allowing  
10 for the majority of operations (including system and compressor startup, cooling the chamber,  
11 icing the walls, and running the activation experiments described in Section 3.1) to be automated  
12 for increased experimental reproducibility. In addition to the foreground sequences initiated by  
13 the user, background sequences can also be run to monitor instrument performance. With remote  
14 access enabled through a virtual network computing server (separate from the LabView  
15 software), much of the chamber operation can be performed remotely.

16

### 17 **3. Methodology**

#### 18 **3.1 Experimental methods**

19 Before beginning experiments, the chamber is dried, cooled, and the walls are coated with  
20 ice. This is accomplished by first flowing dry nitrogen through the chamber via the sample and  
21 sheath flow inlets to remove residual moisture; the flow exiting the chamber outlet is routed  
22 through a dew point sensor, so the moisture content of the chamber can be directly measured to  
23 ensure the dew point is below  $-40^{\circ}\text{C}$ . The compressor system is then activated to cool the



1 chamber to the icing temperature of  $-25^{\circ}\text{C}$ . Before icing, the double distilled deionized 18.2 M $\Omega$   
2 Millipore (DDI) water in the reservoir is cooled to  $\sim 2^{\circ}\text{C}$  to reduce strain on the refrigeration  
3 system during icing and to ensure that the wall temperatures do not exceed  $0^{\circ}\text{C}$  over the course  
4 of the icing process. With the water reservoir attached to the two-way water pump, the “icing  
5 sequence” is activated in the software. This sequence controls the filling and emptying of the  
6 chamber with DDI water to form the ice layers. The “ice dwell counter” in software specifies the  
7 amount of time the chamber is filled with water and is typically set to 5 s. During and after the  
8 icing sequence it is critical to prevent moist room air from entering the chamber, which can  
9 cause non-uniform ice on the chamber walls via the formation of frost. This is accomplished by  
10 flowing dry air or nitrogen through the sample and sheath flow inlets while allowing the excess  
11 flow pressure to be released into the room upstream of the chamber inlets. The entire filling  
12 sequence typically lasts  $\sim 5$  min. After the ice layer has been formed, the dry nitrogen flow  
13 through the chamber is continued to ensure that no frost accumulates in the chamber. Subsequent  
14 installation of the detector and activation of the sheath pump allows for assessment of  
15 background frost counts that may bias the reported INP concentrations. This background  
16 concentration (typically a few counts per liter) sets the lower detection limit of INP and must  
17 ideally be  $< 0.1\%$  of the INP concentration intended to be measured.

18 Once the chamber is iced and has a sufficiently low background, it is ready to perform  
19 activation experiments of INP. This is accomplished in one of two main ways: (1) ramping the  
20 wall temperatures to determine the temperature and/or supersaturation dependent ice crystal  
21 concentration or (2) keeping the walls at different but constant temperatures to measure the time  
22 dependence of ice crystal concentration at desired temperature and supersaturation conditions.  
23 For the former, diverging the wall temperatures increases the chamber supersaturation,



1 converging the wall temperatures decreases chamber supersaturation, and ramping both walls  
2 allows for temperature scans at the same supersaturation. In all cases, the OPC reports side  
3 scatter (sizing) and backscatter (depolarization) spectra to infer size, concentration, and phase of  
4 counted particles.

5 Frost shed from the chamber walls can grow large enough to be counted by the detector, and  
6 this phenomenon is more frequent at higher supersaturations. If the number of frost counts is  
7 comparable to the number of real counts (i.e., on order with the concentration of INPs), the data  
8 collected will include a significant artifact. Therefore, periodically measuring the background  
9 frost counts with no particles in the chamber (by setting the inlet valve to the filter position) is an  
10 important procedure during activation experiments (described below). For converging and  
11 diverging wall temperature ramps, this check is performed at the beginning and end of each  
12 ramp. For constant supersaturation experiments, this check is performed at fixed time intervals,  
13 typically twice per hour. Experiments are automatable using sequences in the SPIN software.  
14 These sequences automate the periodic background checks as well as controlling the wall  
15 temperature set points. The background concentration increases over time as vapor is transferred  
16 from the warm wall to the cold wall, leading to irregularities in the ice layers: as a result, the  
17 experiment must be ended once it no longer meets the required levels. The exact time this occurs  
18 depends on the particular operating conditions for an experiment but is typically after 2-5 hours  
19 of operation.

20 If the temperature gradient between the warm and cold walls is large (e.g. larger than ~ 10-  
21 15°C, depending on the actual temperatures) the buoyancy of the air adjacent to the warm wall is  
22 predicted to overcome the mean flow and causes (upward) flow reversal along the warm wall  
23 (Rogers, 1988). The dashed line in the top panel of Figure 5 shows the supersaturation level



1 above which flow reversal is possible according to the calculations from Rogers (1988), and the  
2 bottom panels show two examples of normal and reversed flow profiles. If flow reversal  
3 interferes with the aerosol lamina, the chamber behavior may deviate from ideality (Rogers,  
4 1988; Stetzer et al., 2008). Increasing the sheath flow combats flow reversal, but it decreases the  
5 residence time of particles in the chamber, which reduces nucleation and crystal growth  
6 efficiencies (Rogers, 1988).

7

### 8 **3.2 Data processing methods**

9 The temperature and supersaturation conditions in the chamber are calculated assuming a  
10 linear temperature and water vapor partial pressure gradient between the walls. The width and  
11 location of the aerosol lamina (and therefore the range of temperatures and supersaturations  
12 experienced by the aerosols) is calculated using the method from Rogers, (1988) using the  
13 reported values for wall temperatures, sheath flow rate, and sample flow rate. This approach  
14 provides a basis for calculating chamber conditions at each pair of thermocouples (on the warm  
15 and cold wall, respectively, at a given location). The flow rates and temperature conditions are  
16 used to calculate the velocity profile, and the ratio of the sample flow rate to the total flow rate is  
17 used to determine the width of the aerosol lamina (Rogers, 1988; Kulkarni and Kok, 2012). Since  
18 a velocity profile calculation is part of this procedure, the fraction of reversed flow is known.

19 The above calculations provide temperatures and supersaturations as a time series along with  
20 the size distributions and depolarization data measured by the OPC, which provides four values  
21 (one from each of the detectors) on a single particle basis. The number of aerosol particles that  
22 have activated into ice crystals or droplets is inferred in post-processing from the classification of  
23 the particle-by-particle data in the four-dimensional OPC parameter space via supervised



1 machine learning. This process is described below and illustrated in Figure 6 for an example  
2 freezing experiment.

3 Machine learning algorithms provide accurate, reproducible, and uncertainty-quantifying  
4 analysis of the OPC data. They also require fewer assumptions to be made about particle  
5 detection and allow more flexibility in experimental design. CFDC OPC data has historically  
6 been analyzed using particle size as the sole determiner of activation into ice or droplets, since  
7 ice crystals grow to be much larger than the seed particles (e.g. Rogers et al., 2001; DeMott et  
8 al., 2010; Chou et al., 2011). If particles larger than a certain size are assumed to be ice crystals,  
9 then it must either be assumed or imposed that all aerosol particles are smaller than the ice size  
10 and that droplets do not survive the evaporation section. In order to meet this constraint, particle  
11 impactors are often used to prevent the largest (and potentially most ice active) particles from  
12 entering the CFDC (e.g. Rogers et al., 2001; DeMott et al., 2010; DeMott et al., 2015). Also, if  
13 the main chamber is supersaturated with respect to water, the aerosol particles may activate into  
14 droplets. The evaporation section is designed to avoid counting these droplets in the OPC, but it  
15 will cease to efficiently evaporate droplets above a threshold (temperature-dependent)  
16 supersaturation level. This droplet breakthrough threshold typically provides an upper limit for  
17 measurable supersaturation, above which droplets must be differentiated from ice crystals, and it  
18 marks the upper RH limit for traditional CFDC operation and data analysis. However, the  
19 addition of depolarization data and analysis using supervised machine learning algorithms allow  
20 for this size assumption to be relaxed, since all detected particles are classified by phase and the  
21 uncertainty associated with this classification is quantified (see below).

22 Supervised machine learning algorithms require that the different output classes (in this case,  
23 aerosol particles, water droplets, and ice crystals) have corresponding training data (Mohri et al.,



1 2012). However, the SPIN OPC data from an activation experiment typically contains mixtures  
2 of these classes rather than the pure end members, so training data must be sampled from some  
3 subset of the parameter space that represents the different classes. In order to inform this  
4 sampling, Kernel Density Estimation (KDE) is used to create probability density functions  
5 (PDFs) of the data in various time intervals. The SPIN OPC reports four values (size, S1, P1, and  
6 P2) in the Particle-by-Particle (PbP) data, and KDE with automatic bandwidth estimation  
7 (Kristan et al., 2011) is used to create a 4-dimensional Gaussian mixture model (GMM) of the  
8 PDF's for this particle data. Figure 6 shows data from an illite NX freezing experiment at -40°C  
9 with ramping supersaturation. Specifically, Figure 6a shows PbP data from the beginning of the  
10 experiment during an “aerosol only” time interval (time 1) and the corresponding KDE (for ease  
11 of visualization the 2D GMM-KDE in S1/P1 vs. size parameter space shown in lieu of the full  
12 4D GMM-KDE). Figure 6b similarly shows data and the GMM-KDE during an “aerosol + ice”  
13 time interval (time 2, at a supersaturation higher than that required for the onset of ice  
14 formation). The PDF in Figure 6a is subtracted from the one in Figure 6b and is used to create a  
15 residual PDF, which is then used to inform the weighted sampling of data from time 2 to create  
16 training data for the “ice only” output class (Figure 6c). The data corresponding to the “aerosol  
17 only” (Figure 6a) and “ice only” (Figure 6c) classes are then used to train a Gaussian kernel  
18 support vector machine (SVM), and classification uncertainties are quantified via 5-fold cross  
19 validation of the training data (Figure 6d). Once trained, the SVM classifies the OPC data from  
20 an experiment with a known missed classification percentage (Figure 6e). Since a condensation  
21 particle counter (CPC) is typically used in parallel to SPIN to measure the concentration of  
22 particles entering the chamber, this estimate of the number of ice crystals is used to infer



1 activated fractions by dividing the inferred ice crystal concentration by the total particle  
2 concentration entering the chamber.

3 Figure 7 shows an extension of this approach to discriminate aerosol particles, water droplets  
4 and ice crystals using an application of 3-class supervised machine learning (bootstrap  
5 aggregated decision trees are used for the classification algorithm instead of SVM in this case)  
6 on an example (dry-generated, polydisperse) silver iodide (AgI) activation experiment at -17°C  
7 where the chamber RH is increased. Though a 4D parameter space is again used for this  
8 classification, Figure 7a shows only three of the PbP data dimensions along with 2D projections  
9 at the axes limits to illustrate the portions of the parameter space occupied by each class. With  
10 this approach, the concentrations (Figure 7b) and fractions (Figure 7c) of ice crystals and water  
11 droplets along with classification uncertainty can be reported as a function of chamber  
12 conditions. With the large datasets (thousands of data points per second) generated by the SPIN  
13 OPC, accurate particle classification is performed in a reproducible manner with validation  
14 accuracies of 95.0-99.9%.

15

#### 16 **4. Results and comparisons to literature**

17 To evaluate the performance of the SPIN OPC, sizing and detection experiments are  
18 performed with different sizes of monodisperse spheres. Glass beads, polystyrene latex spheres,  
19 and melamine resin spheres are used for the characterizations. The results from these validations  
20 are shown in Figure 8, and illustrate how the SPIN OPC sizes particles (Figure 8a). The sizing  
21 behavior follows a power law fit for particle sizing between 0.5 and 11  $\mu\text{m}$ . Smaller particles  
22 scatter the laser light less efficiently, and decreasing detection efficiency with decreasing size is



1 observed for sub-micrometer particles (Figure 8b). In the super-micrometer size range (where ice  
2 crystals are expected to be present) the counting efficiency is very close to 1.

3 To evaluate the behavior of the SPIN chambers, several types of freezing experiments are  
4 reported. Specifically, 200nm (nebulized, dried, and mobility selected) ammonium sulfate (AS)  
5 aerosol is used to determine the droplet breakthrough line and to compare the homogeneous  
6 freezing points reported by SPIN to literature values. Also, polydisperse, dry-generated NX illite  
7 and AgI (Sigma Aldrich 99%) particles are used to investigate the heterogeneous ice activation  
8 for comparison to literature. The homogeneous freezing results shown in Figure 9 suggest that  
9 the temperatures and supersaturations reported by SPIN are indicative of the real conditions in  
10 the chamber. Similarly, the results from the heterogeneous freezing experiments are shown in  
11 Figure 10 and indicate freezing occurs in the expected regions of phase space for the different  
12 seed particles.

13 AS data is used to characterize SPIN's behavior in humid (near or above water saturation)  
14 conditions across a wide range of temperatures. AS freezing experiments at colder temperatures  
15 provide validation for the chamber performance against the well-characterized homogeneous  
16 freezing behavior. The data in Figure 9 show that this behavior is captured in both temperature  
17 and RH ramps and occurs in the expected region of phase space. They demonstrate that droplets  
18 in SPIN begin to freeze when the chamber temperature falls below  $\sim -38^{\circ}\text{C}$  and that  
19 homogeneously frozen ice crystals begin to disappear above this temperature. Similarly, the RH  
20 ramp data show that supercooled aqueous AS solutions freeze at RH levels similar to those  
21 predicted by Koop et al., (2000).

22 At warmer temperatures, homogeneous freezing does not occur, so AS is used to measure  
23 SPIN's droplet breakthrough threshold. Though post processing of the PbP detector data can



1 distinguish droplets from ice (Section 3.2), droplet breakthrough is quantified using AS (which is  
2 much more hygroscopic than many INP's) provides a conservative (lower RH) estimate for  
3 where this occurs. The measured droplet breakthrough line indicates that SPIN's evaporation  
4 section significantly extends (a few percent above water saturation) the region of phase space  
5 where experiments can be performed without needing to differentiate droplets from ice crystals.

6 AgI, despite not being found in the atmosphere, freezes very efficiently in the deposition  
7 mode across a range of temperatures and provides a benchmark to assess chamber performance  
8 (Detwiler and Vonnegut, 1981; Stetzer et al., 2008). The SPIN results shown in Figure 10 match  
9 literature data across a wide temperature range and demonstrate that SPIN accurately captures  
10 ice nucleation at warmer temperatures where there are many atmospherically relevant INP that  
11 activate into ice crystals. In addition to AgI results, heterogeneous freezing results for NX illite  
12 and kaolinite are also included, because they are commonly used surrogates for atmospheric  
13 dust, which is important for ice nucleation at colder temperatures (DeMott et al., 2003b; Welti et  
14 al., 2009; Cziczo et al., 2013). Unlike AgI, NX illite and kaolinite show a strong temperature  
15 dependence in freezing behavior and nucleate ice much less efficiently at temperatures warmer  
16 than  $\sim -35^{\circ}\text{C}$ . Previous investigation of these materials has shown this transition (e.g., Welti et al.,  
17 2009), and the SPIN data in this study also captures this temperature dependence. Additionally,  
18 the coldest illite data points show that SPIN can access temperatures in the cirrus cloud regime,  
19 which are typically too cold for portable CFDC chambers to measure (Rogers et al., 2001; Chou  
20 et al., 2011).

21

## 22 **5. Quantifying uncertainty**



1 With a CFDC instrument, there are various sources of uncertainty that influence  
2 experimental results (e.g. Rogers, 1988; Stetezer et al., 2008). Uncertainties in wall temperatures,  
3 flows, numbers of counted ice crystals, flow reversal, and other deviations from ideality must be  
4 considered when interpreting results from a CFDC chamber. In SPIN, wall temperatures are  
5 recorded at sixteen locations on each wall. The aerosol lamina temperature and supersaturation  
6 conditions are calculated based on the measurements at these locations, providing a way to infer  
7 the variations in thermodynamic conditions experienced by the aerosol. Since the three  
8 bottommost thermocouples are strongly coupled to the evaporation section and occupy the  
9 transition region between the moist main chamber and dry evaporation section, only the top  
10 thirteen thermocouples are used for reporting chamber conditions. Therefore, uncertainty in  
11 chamber conditions is reported as the standard deviation of the lamina temperature and relative  
12 humidity at these thirteen locations. Variability in the wall temperatures depends on operating  
13 conditions (but typically have standard deviations of 0.5-2°C), and these variations must be  
14 included in uncertainty estimates. Along with these temperature gradients, variations in  
15 temperature and supersaturation across the width of the aerosol lamina are sources of uncertainty  
16 in SPIN measurements. Also, classification uncertainty from the machine learning approach is  
17 used for reporting uncertainties in ice crystal concentrations and activated fractions.

18 Computational fluid dynamics (CFD) calculations in this section are used to explore how  
19 closely simulated chamber conditions match ideality. Figure 11 shows results from ANSYS  
20 Fluent CFD modeling (Fluent, 2015) of the SPIN chamber. Several simulations were performed  
21 and results from two of these are shown. Specifically, the left column in Figure 11 shows results  
22 for nominal lamina temperature of -40°C and lamina  $S_{ice}$  at 1.3, and the right column shows  
23 results for nominal lamina temperature of -30°C and lamina  $S_{ice}$  at 1.1. Overall, simulated



1 chamber temperature, RH, and flow velocity match the ideal case predicted by Rogers (1988) for  
2 these and other Fluent experiments. Flow reversal along the warm wall (Figure 5) is also  
3 observed in high RH simulations, but as with the physical experiments, this effect does not  
4 appear to have an appreciable influence on the aerosol lamina conditions beyond that which is  
5 predicted by Rogers (1988) model. Since the analytical and CFD models show qualitatively  
6 similar flow reversal, this effect is accounted for when reporting chamber conditions with the  
7 analytical model. Furthermore, agreement between the homogeneous freezing data and expected  
8 homogeneous freezing conditions provides evidence that this effect does not bias results, since  
9 these experiments are performed where a large degree of flow reversal is expected.

10

## 11 **6. Conclusions**

12 This study outlines the theoretical principles, chamber design, and experimental validation of  
13 the SPIN chamber, a commercially available CFDC chamber manufactured by Droplet  
14 Measurement Technologies (DMT). The results from this study validate the SPIN chamber  
15 performance using a variety of experimental tests and CFD modeling.

16 The introduction of SPIN as a commercially available instrument lowers the barrier of entry  
17 to make INP measurements in a manner similar to the introduction of the DMT CCN Counter  
18 (Roberts and Nenes, 2005; Lance et al., 2006), allowing these measurements to be made with  
19 higher temporal and spatial coverage. In addition, the methodologies highlighted in this study  
20 facilitate INP measurements to be performed with increased experimental flexibility and  
21 reproducibility and also with fewer assumptions in the analysis. In particular, the addition of a  
22 depolarization detector coupled with supervised machine learning algorithms for data analysis  
23 allows for robust determination of particle size and phase with uncertainty quantification.



1 The experiments presented in this study validate SPIN's measurements of freezing behavior  
2 of both heterogeneous and homogeneous INP and demonstrate that the SPIN chamber  
3 reproduces freezing data measured in previous studies. The AgI measurements provide  
4 validation over a wide range of temperatures, extending to regions where the more efficient  
5 atmospheric INP would activate into crystals. The NX illite and kaolinite measurements  
6 demonstrate that SPIN measures into the heterogeneous freezing portion of the cirrus cloud  
7 regime and also captures the temperature dependence of mineral dust ice activity. The AS  
8 experiments provide an estimate of the droplet breakthrough level of the SPIN chamber at  
9 warmer temperatures, and at colder temperatures shows that homogeneous freezing occurs in  
10 agreement with previous experiments and theory. By using an uncertainty quantifying OPC  
11 analysis technique, recording high spatial resolution temperature measurements along the  
12 chamber walls, and investigating the chamber conditions using CFD modeling, the main sources  
13 of uncertainty in SPIN measurements have also been studied.

14 Overall, the SPIN chamber reproduces laboratory data measured by previous CFDC  
15 chambers, and the uncertainties in the measurements have been investigated. SPIN's availability  
16 as a commercially available CFDC chamber increases the opportunities for experimental and  
17 field data to be collected. Such an increase in coverage of INP measurements will help constrain  
18 the influence of ice nucleation on the atmospheric radiation budget and the initiation of  
19 precipitation, thereby leading to a better understanding of the impact of ice formation on the  
20 Earth's climate and water budget.



## 1 **Acknowledgements**

2 The development of the SPIN instrument was supported by the U.S. Department of Energy,  
3 Office of Science, STTR program under Award Number DE-SC-0004258. S. Garimella and D. J.  
4 Cziczo would like to acknowledge NASA Grant NNX13AO15G and the MIT Martin Family  
5 Society for Sustainability for funding. T. B. Kristensen and F. Stratmann gratefully acknowledge  
6 funding from the German Federal Ministry of Education and Research (BMBF) through the  
7 CLOUD-12 project (01LK1222B). K. Ignatius and L. Nichman gratefully acknowledge funding  
8 from the EC seventh Framework Programme (Marie Curie Initial Training Networks MC-ITN  
9 CLOUD-TRAIN grant no. 316662). T. W. Wilson acknowledges funding from the Natural  
10 Environment Research Council (NE/K004417/ 1).

11



## 1 **References**

- 2 Bailey, M. and Hallett, J.: Nucleation effects on the habit of vapour grown ice crystals from –18  
3 to –42°C, *Q. J. Roy. Meteor. Soc.*, 128, 1461–1483, doi:10.1256/00359000260247318,  
4 2002.
- 5 Boucher, O., Randall, D., Artaxo, P., Bretherton, C., Feingold, G., Forster, P., Kerminen, V.-M.,  
6 Kondo, Y., Liao, H., Lohmann, U., Rasch, P., Satheesh, S., Sherwood, S., Stevens, B.,  
7 and Zhang, X.: Clouds and aerosols, in: *Climate Change 2013: The Physical Science*  
8 *Basis, Working Group I Contribution to the Fifth Assessment Report of the*  
9 *Intergovernmental Panel on Climate Change*, Cambridge, United Kingdom and New  
10 York, NY, USA, 571-657, 2013.
- 11 Chen, Y. L., Kreidenweis, S. M., McInnes, L. M., Rogers, D. C., and DeMott, P. J.: Single  
12 particle analyses of ice nucleating aerosols in the upper troposphere and lower  
13 stratosphere, *Geophys. Res. Lett.*, 25, 1391-1394, 10.1029/97gl03261, 1998.
- 14 Chou, C., Stetzer, O., Weingartner, E., Juranyi, Z., Kanji, Z. A., and Lohmann, U.: Ice nuclei  
15 properties within a Saharan dust event at the Jungfrauoch in the Swiss Alps, *Atmos.*  
16 *Chem. Phys.*, 11, 4725-4738, 10.5194/acp-11-4725-2011, 2011.
- 17 Chou, C., Kanji, Z. A., Stetzer, O., Tritscher, T., Chirico, R., Heringa, M. F., Weingartner, E.,  
18 Prevot, A. S. H., Baltensperger, U., and Lohmann, U.: Effect of photochemical ageing on  
19 the ice nucleation properties of diesel and wood burning particles, *Atmos. Chem. Phys.*,  
20 13, 761-772, 10.5194/acp-13-761-2013, 2013.
- 21 Clauss, T., A. Kiselev, S. Hartmann, S. Augustin, S. Pfeifer, D. Niedermeier, H. Wex, and F.  
22 Stratmann: Application of linear polarized light for the discrimination of frozen and



- 1 liquid droplets in ice nucleation experiments, *Atmos. Meas. Tech.*, 6, 1041-1052,  
2 doi:10.5194/amt-6-1041-2013, 2013.
- 3 Cziczo, D. J., Froyd, K. D., Hoose, C., Jensen, E. J., Diao, M., Zondlo, M. A., Smith, J. B.,  
4 Twohy, C. H., and Murphy, D. M.: Clarifying the dominant sources and mechanisms of  
5 cirrus cloud formation, *Science*, 340, 1320–1324, 2013.
- 6 DeMott, P. J., Cziczo, D. J., Prenni, A. J., Murphy, D. M., Kreidenweis, S. M., Thomson, D. S.,  
7 Borys, R., and Rogers, D. C.: Measurements of the concentration and composition of  
8 nuclei for cirrus formation, *P. Natl. Acad. Sci. USA*, 100, 14655-14660,  
9 10.1073/pnas.2532677100, 2003a.
- 10 DeMott, P. J., Sassen, K., Poellot, M. R., Baumgardner, D., Rogers, D. C., Brooks, S. D., Prenni,  
11 A. J., and Kreidenweis, S. M.: African dust aerosols as atmospheric ice nuclei, *Geophys.*  
12 *Res. Lett.*, 30, 10.1029/2003gl017410, 2003b.
- 13 DeMott, P.J., Prenni, A. J., Liu, X., Petters, M. D., Twohy, C. H., Richardson, M. S.,  
14 Eidhammer, T., Kreidenweis, S. M., and Rogers, D. C.: Predicting global atmospheric ice  
15 nuclei distributions and their impacts on climate, *P. Natl. Acad. Sci. USA*, 107, 11217-  
16 11222, 2010.
- 17 DeMott, P. J., Prenni, A. J., McMeeking, G. R., Sullivan, R. C., Petters, M. D., Tobo, Y.,  
18 Niemand, M., Möhler, O., Snider, J. R., Wang, Z., and Kreidenweis, S. M.: Integrating  
19 laboratory and field data to quantify the immersion freezing ice nucleation activity of  
20 mineral dust particles, *Atmos. Chem. Phys.*, 15, 393-409, doi:10.5194/acp-15-393-2015,  
21 2015.
- 22 Detwiler, A. G. and Vonnegut, B.: Humidity required for ice nucleation from the vapor onto  
23 silver iodide and lead iodide aerosols over the temperature range  $-6$  to  $-67^{\circ}\text{C}$ , *J. Appl.*



- 1 Meteorol., 20, 1006–1012, doi:10.1175/1520-0450(1981)020<1006:HRFINF>2.0.CO;2,  
2 1981.
- 3 Fluent 16.0 User’s Guide. ANSYS Inc., Cecil Township, PA, USA, 2015.
- 4 Friedman, B., Zelenyuk, A., Beranek, J., Kulkarni, G., Pekour, M., Hallar, A. G., McCubbin, I.  
5 B., Thornton, J. A., and Cziczo, D. J.: Aerosol measurements at a high-elevation site:  
6 composition, size, and cloud condensation nuclei activity, Atmos. Chem. Phys., 13,  
7 11839-11851, 10.5194/acp-13-11839-2013, 2013.
- 8 Kanji, Z. A., and Abbatt, J. P. D.: The University of Toronto Continuous Flow Diffusion  
9 Chamber (UT-CFDC): A Simple Design for Ice Nucleation Studies, Aerosol Sci. Tech.,  
10 43, 730-738, 10.1080/02786820902889861, 2009.
- 11 Kanji, Z. A., Welti, A., Chou, C., Stetzer, O., and Lohmann, U.: Laboratory studies of immersion  
12 and deposition mode ice nucleation of ozone aged mineral dust particles, Atmos. Chem.  
13 Phys., 13, 9097-9118, 10.5194/acp-13-9097-2013, 2013.
- 14 Koop, T., Luo, B. P., Tsias, A., and Peter, T.: Water activity as the determinant for homogeneous  
15 ice nucleation in aqueous solutions, Nature, 406, 611–614, doi:10.1038/35020537, 2000.
- 16 Kristan, M., Leonardis, A., and Skocaj, D.: Multivariate online kernel density estimation with  
17 Gaussian kernels, Pattern Recogn., 44, 2630-2642, 10.1016/j.patcog.2011.03.019, 2011.
- 18 Kulkarni, G., Dobbie, S., and McQuaid, J. B.: A new thermal gradient ice nucleation diffusion  
19 chamber instrument: design, development and first results using Saharan mineral dust,  
20 Atmos. Meas. Tech., 2, 221-229, 2009.
- 21 Kulkarni, G., and Kok, G.: Mobile Ice Nucleus Spectrometer, Pacific Northwest National  
22 Laboratory, 2012.



- 1 Lance, S., Medina, J., Smith, J. N., and Nenes, A.: Mapping the operation of the DMT  
2 Continuous Flow CCN counter, *Aerosol Sci. Tech.*, 40, 242-254,  
3 10.1080/02786820500543290, 2006.
- 4 Liou, K. N., and Lahore, H.: Laser Sensing of Cloud Composition – Backscattered  
5 Depolarization Technique, *J. Appl. Meteorol.*, 13, 257-263, 10.1175/1520-  
6 0450(1974)013<0257:lsocca>2.0.co;2, 1974.
- 7 Lüönd, F., Stetzer, O., Welti, A., and Lohmann, U.: Experimental study on the ice nucleation  
8 ability of size-selected kaolinite particles in the immersion mode, *J. Geophys. Res.-*  
9 *Atmos.*, 115, 10.1029/2009jd012959, 2010.
- 10 Mason, B., and van den Heuvel, A.: The Properties and Behavior of Some Artificial Ice Nuclei,  
11 *Proc. Phys. Soc.*, 74, 744–755, 1958.
- 12 Mohri, M., Rostamizadeh, A., and Talwalkar, A.: *Foundations of Machine Learning*, MIT Press,  
13 Cambridge, MA, USA, 2012.
- 14 Niehman, L., Fuchs, C., Järvinen, E., Ignatius, K., Höppel, N. F., Dias, A., Heinritzi, M., Simon,  
15 M., Tröstl, J., Wagner, A. C., Wagner, R., Williamson, C., Yan, C., Bianchi, F.,  
16 Connolly, P. J., Dorsey, J. R., Duplissy, J., Ehrhart, S., Frege, C., Gordon, H., Hoyle, C.  
17 R., Kristensen, T. B., Steiner, G., Donahue, N. M., Flagan, R., Gallagher, M. W., Kirkby,  
18 J., Möhler, O., Saathoff, H., Schnaiter, M., Stratmann, F., and Tomé, A.: Discrimination  
19 of water, ice and aerosols by light polarisation in the CLOUD experiment, *Atmos. Chem.*  
20 *Phys. Discuss.*, 15, 31433-31469, doi:10.5194/acpd-15-31433-2015, 2015.

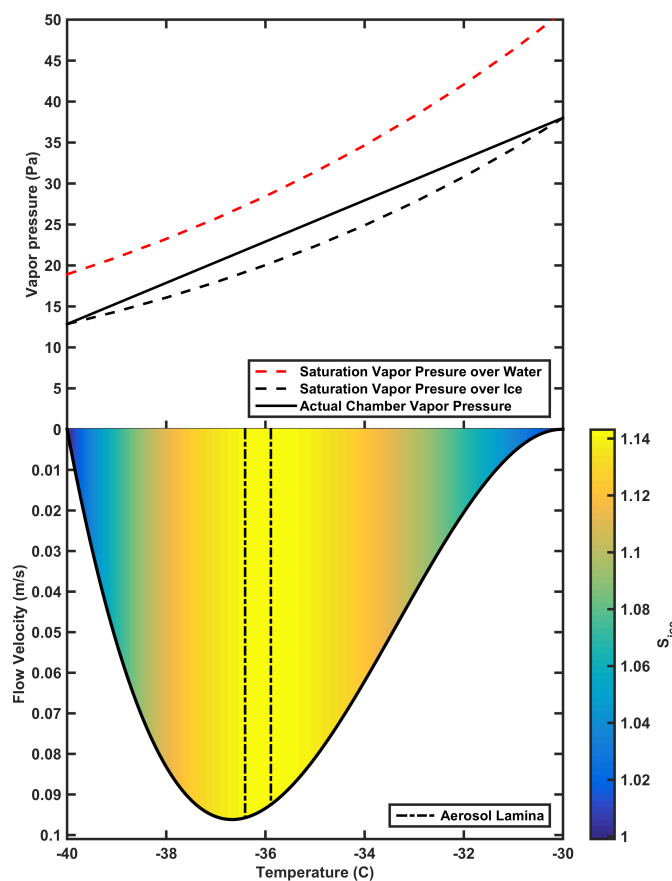


- 1 Nicolet, M., Stetzer, O., Lüönd, F., Möhler, O., and Lohmann, U.: Single ice crystal  
2 measurements during nucleation experiments with the depolarization detector IODE,  
3 Atmos. Chem. Phys., 10, 313-325, 2010.
- 4 Petters, M. D., and Kreidenweis, S. M.: A single parameter representation of hygroscopic growth  
5 and cloud condensation nucleus activity, Atmos. Chem. Phys., 7, 1961-1971, 2007.
- 6 Pruppacher, H. R. and Klett, J. D.: Microphysics of Clouds and Precipitation, Atmospheric and  
7 oceanographic sciences library, Kluwer Academic Publishers, Dordrecht, The  
8 Netherlands, 2<sup>nd</sup> ed., 1997.
- 9 Roberts, G. C., and Nenes, A.: A continuous-flow streamwise thermal-gradient CCN chamber  
10 for atmospheric measurements, Aerosol Sci. Tech., 39, 206-221,  
11 10.1080/027868290913988, 2005.
- 12 Rogers, D. C.: Development of a continuous flow thermal gradient diffusion chamber for ice  
13 nucleation studies, Atmos. Res., 22, 149-181, 1988.
- 14 Rogers D. C., DeMott P. J., Kreidenweis S. M., and Chen Y. L.: A continuous-flow diffusion  
15 chamber for airborne measurements of ice nuclei. J. Atmos. Ocean Tech. 18, 725–741,  
16 2001.
- 17 Saito, A., Murakami, M., and Tanaka, T.: Automated Continuous-Flow Thermal-Diffusion-  
18 Chamber Type Ice Nucleus Counter, SOLA, 7, 29-32, 2011.
- 19 Salam, A., Lesins, G., and Lohmann, U.: Laboratory study of heterogeneous ice nucleation in  
20 deposition mode of montmorillonite mineral dust particles aged with ammonia, sulfur  
21 dioxide, and ozone at polluted atmospheric concentrations, Air Qual. Atmos. Health, 1,  
22 135-142, 10.1007/s11869-008-0019-6, 2008.

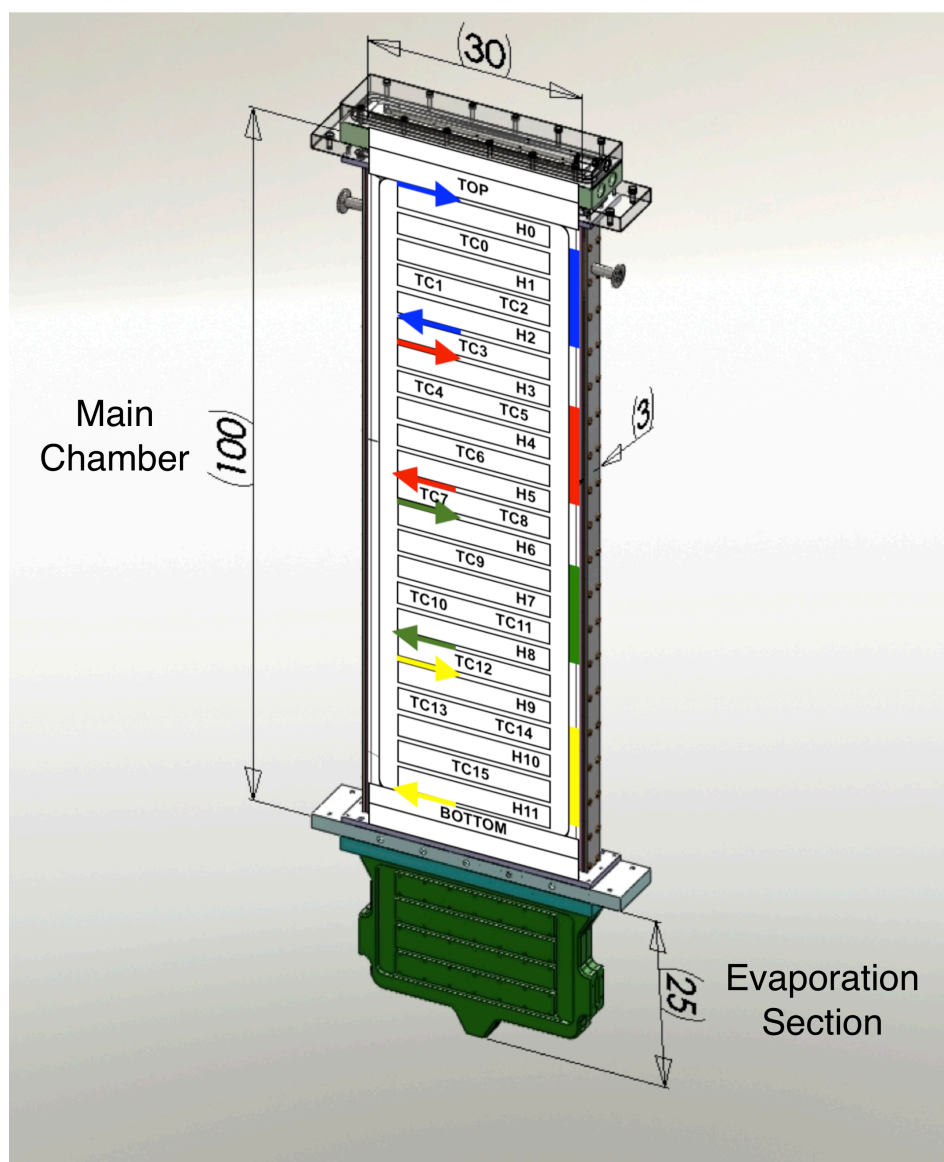


- 1 Stetzer, O., Baschek, B., Lüönd, F., and Lohmann, U.: The Zurich Ice Nucleation Chamber  
2 (ZINC) - A new instrument to investigate atmospheric ice formation, *Aerosol Sci.*  
3 *Technol.*, 42, 64-74, 10.1080/02786820701787944, 2008.
- 4 Stocker, T., Qin, D., and Platner, G.: *Climate Change 2013: The Physical Science Basis,*  
5 *Working Group I Contribution to the Fifth Assessment Report of the Intergovernmental*  
6 *Panel on Climate Change. Summary for Policymakers (IPCC, 2013), Cambridge, United*  
7 *Kingdom and New York, NY, USA, 2013.*
- 8 Welti, A., Lüönd, F., Stetzer, O., and Lohmann, U.: Influence of particle size on the ice  
9 nucleating ability of mineral dusts, *Atmos. Chem. Phys.*, 9, 6705-6715, 2009.
- 10 Welti, A., Kanji, Z. A., Lüönd, F., Stetzer, O., Lohmann, U.: Exploring the Mechanisms of Ice  
11 Nucleation on Kaolinite: From Deposition Nucleation to Condensation Freezing, *J.*  
12 *Atmos. Sci.*, 71, 16-36, 2014.

13



1  
2 Figure 1. Representation of idealized chamber thermodynamic and flow conditions with chamber  
3 width of 1 cm. The chamber cold wall (left) temperature is  $-40^{\circ}\text{C}$  and chamber warm wall (right)  
4 is  $-30^{\circ}\text{C}$ . The top half of the figure shows the saturation vapor pressures over ice (black dashed  
5 line), over water (red dashed line), and chamber vapor pressure (solid black line) for 10 Lpm  
6 sheath + 1 Lpm sample flow. Note the chamber is supersaturated everywhere with respect to ice  
7 but subsaturated with respect to water. The bottom half of the figure shows the flow velocity  
8 profile with the aerosol lamina given by the black dash-dotted lines. The colors show the  
9 horizontal variation in the ice saturation ratio across the width of the chamber. The asymmetry in  
10 the flow profile is a result of the buoyant displacement of the flow towards the cold wall.



1

2 Figure 2. SPIN chamber schematic showing dimensions of the chamber with overlaid  
3 thermocouple (TC0-TC15), heater (H0-H11), and refrigeration zone (colored arrows and blocks)  
4 locations on the main chamber. Heater strips span the length of the chamber wall at each  
5 indicated location. The different colored arrows represent different refrigerant paths depending  
6 on which of the four refrigeration solenoid valves are open. All dimensions are in cm.

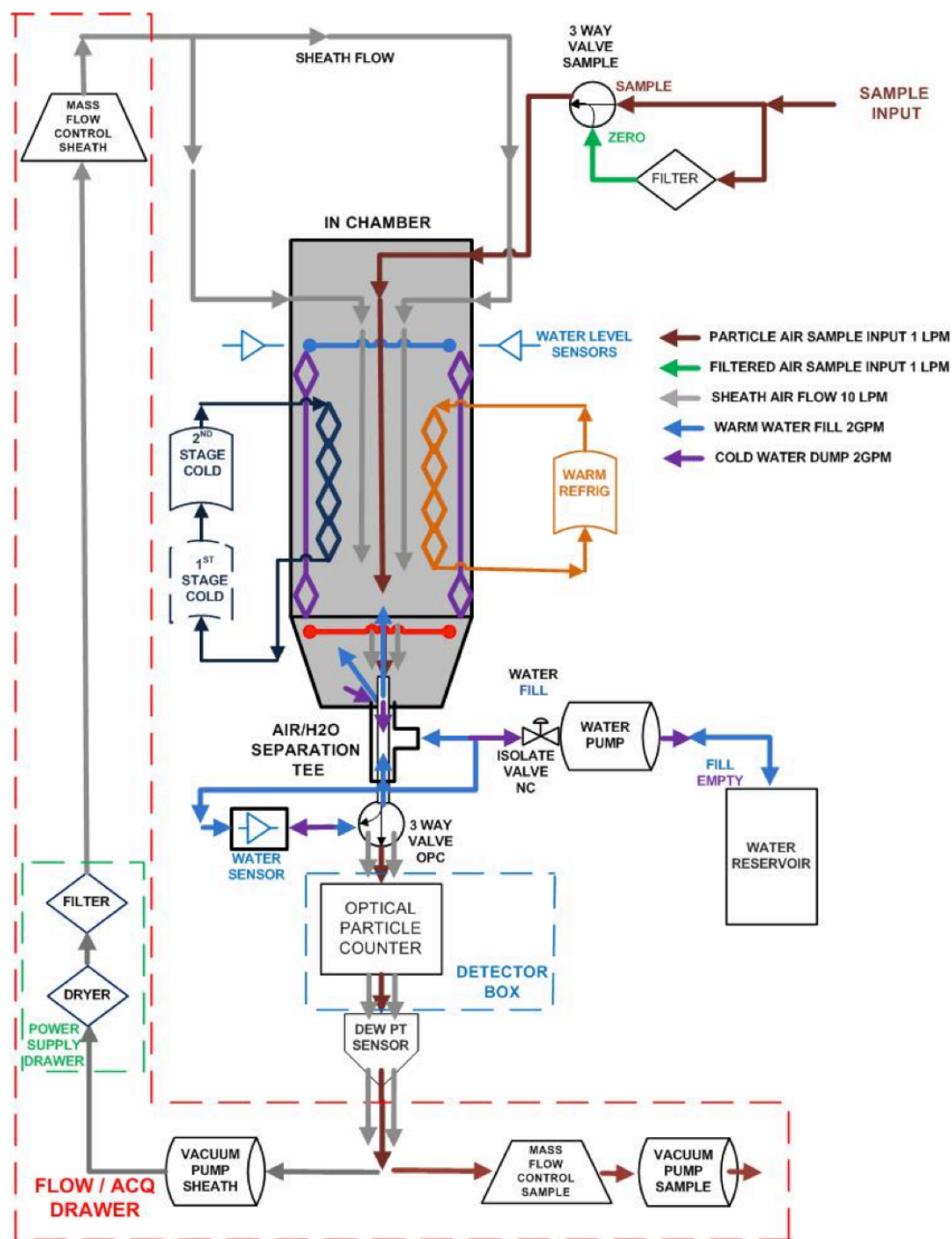
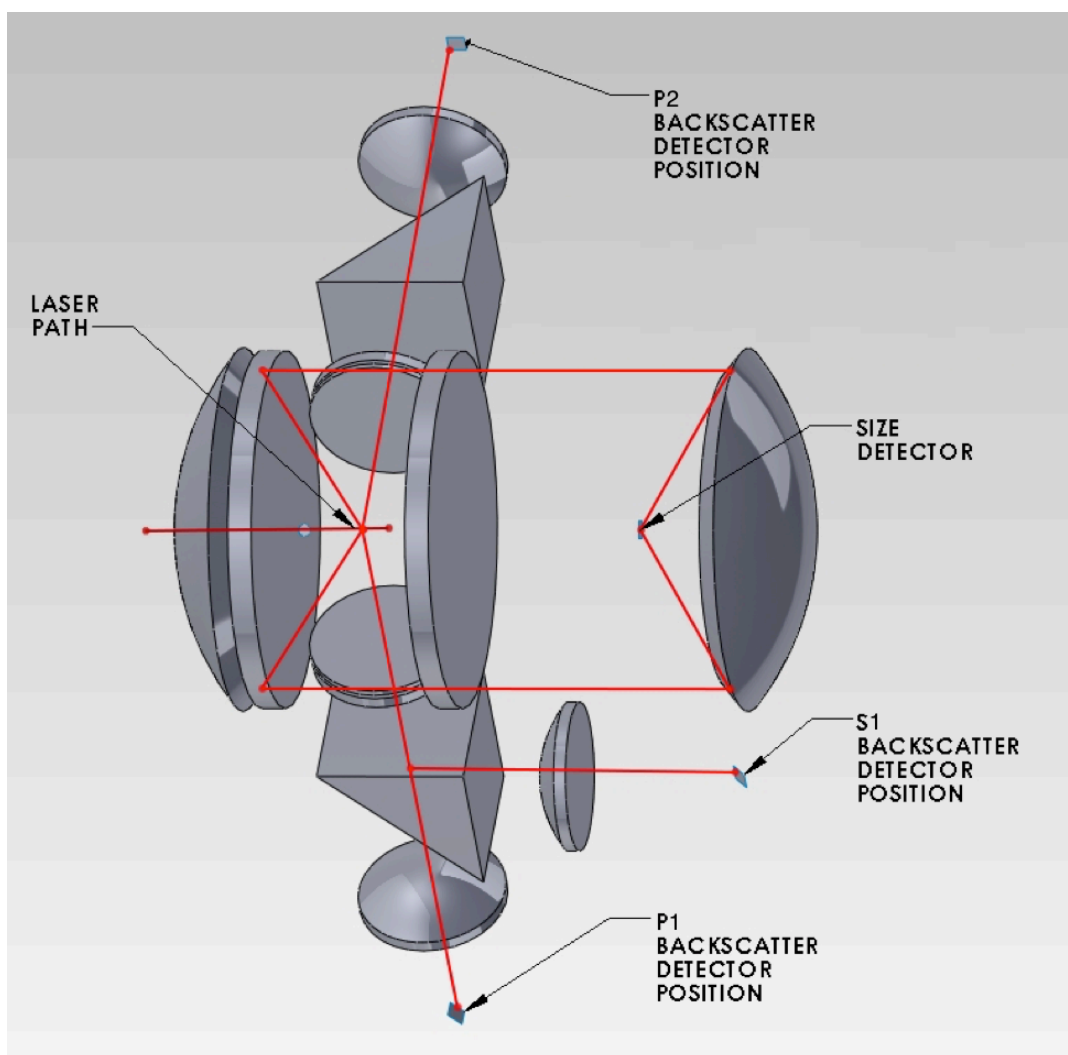
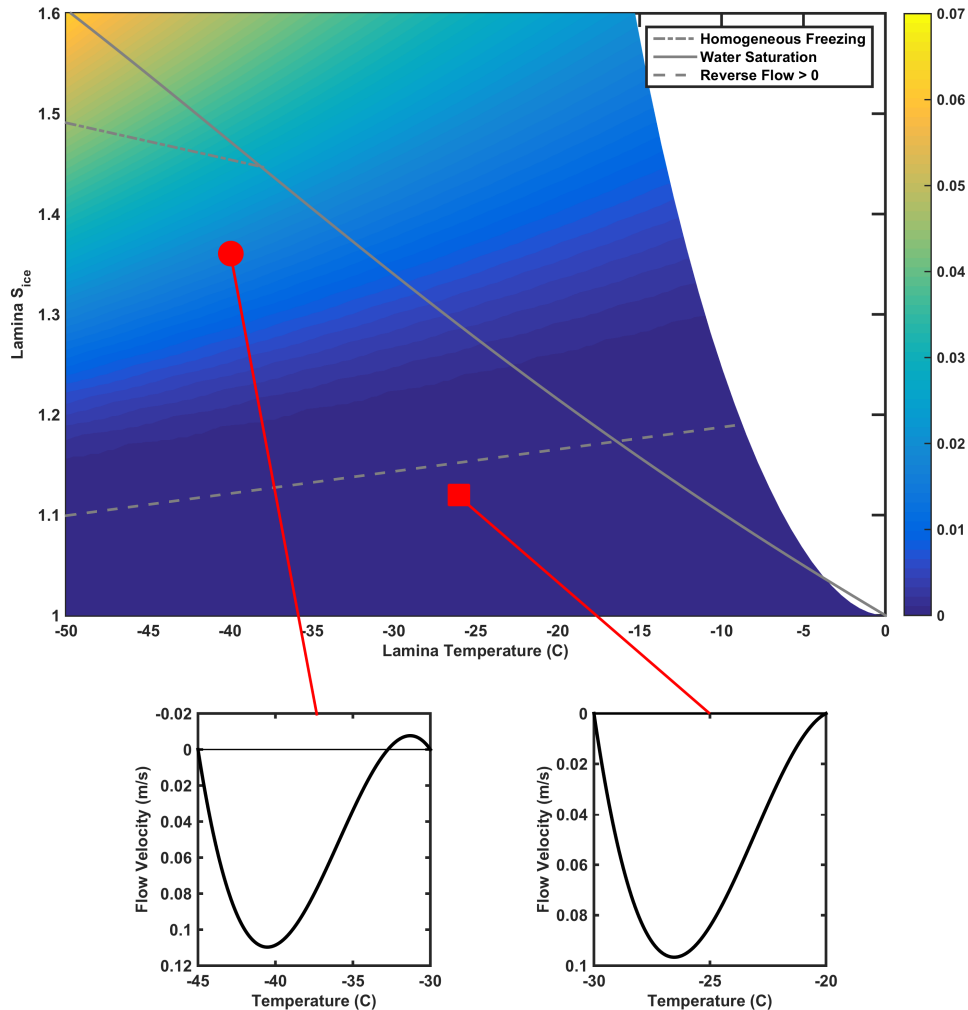


Figure 3. Air and water flow diagram for the SPIN chamber.

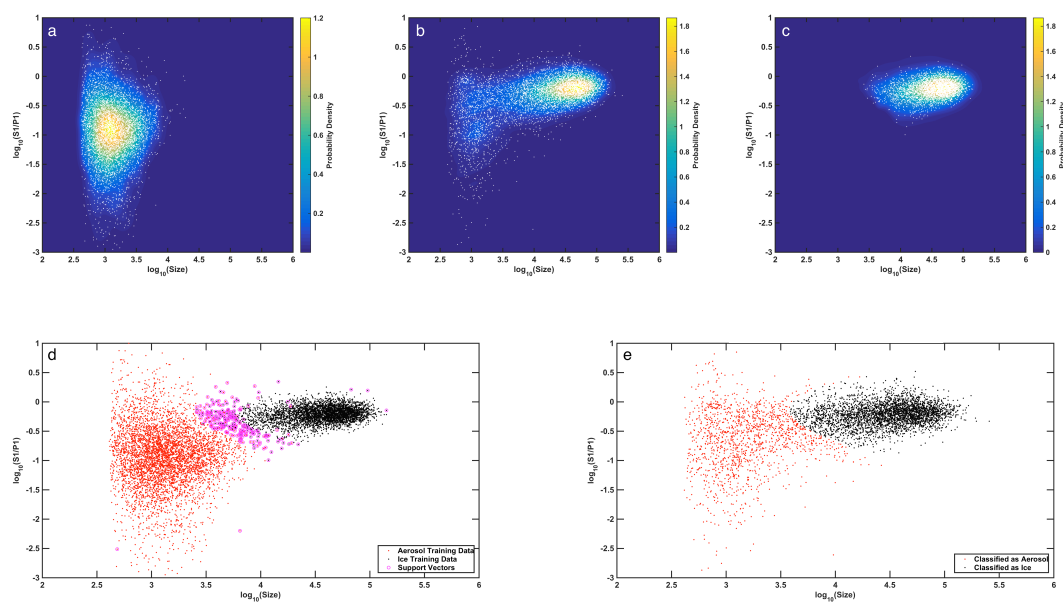


1  
2 Figure 4. Optical schematic of the SPIN OPC. The laser light is shown entering the sampling  
3 region, with side scatter rays travelling to the sizing detector, and the backscatter rays travelling  
4 to the depolarization detectors (see text for details).



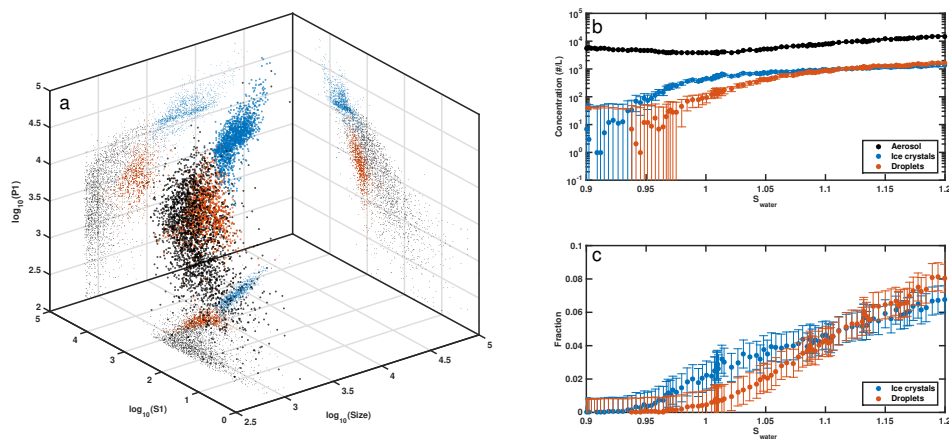
1

2 Figure 5. Phase diagram of ice saturation ratio vs. temperature showing the thermodynamic  
3 conditions accessible by CFDC chambers. The color scale shows the degree of flow reversal  
4 assuming a negligibly thick ice layer predicted by Rogers (1988) with the dashed grey line  
5 marking the boundary between zero and nonzero flow reversal (see text for details). The solid  
6 grey line is water saturation, and the grey dash-dot line shows the onset of homogeneous freezing  
7 from Koop et al. (2000). Two flow profiles are shown: flow reversal occurring along the warm  
8 wall (left, red circle) and no flow reversal (right, red square).



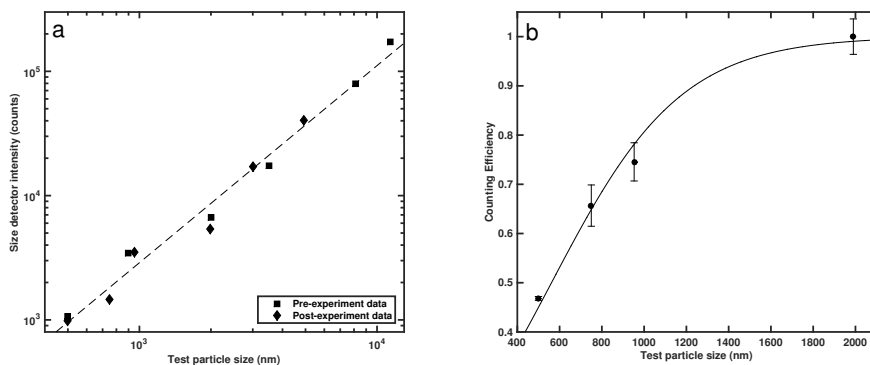
1

2 Figure 6. Illustration of the supervised machine learning procedure used to classify OPC data in  
3  $\log_{10}(S1/P1)$  vs.  $\log_{10}(\text{Size})$  parameter space. (a) Data and GMM-KDE for an “aerosol only” time  
4 interval (time 1). (b) Data and GMM-KDE for an “aerosol + ice” time interval (time 2). (c)  
5 Residual GMM-KDE (time 2 minus time 1) and data from weighted sampling informed by the  
6 residual PDF. (d) Aerosol data, ice data and support vectors for SVM training. Cross validated  
7 classification accuracy is 99% in this example. (e) Data from time 2 classified by SVM as  
8 aerosol and ice. See text for details.

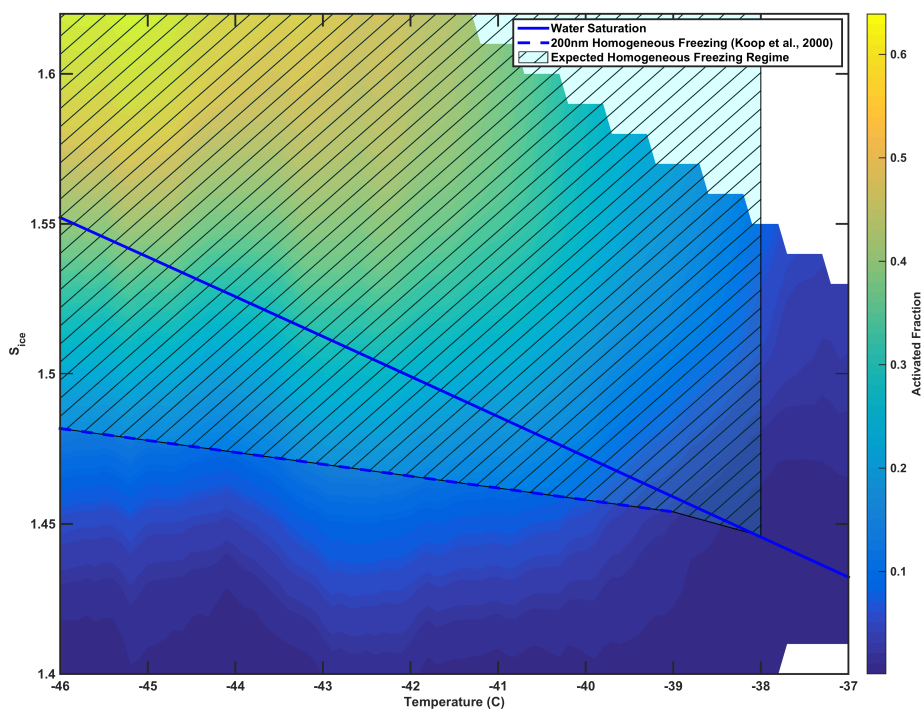


1

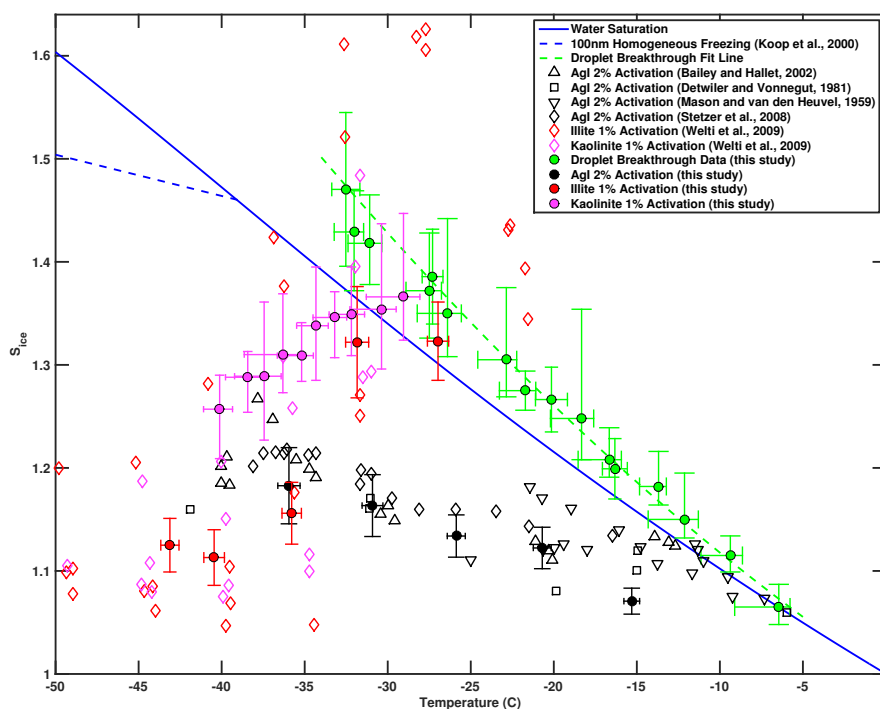
2 Figure 7. Application of 3-class supervised machine learning on an example activation  
3 experiment where the chamber RH is increased. (a) Aerosol particles (black), ice crystals (blue),  
4 and water droplets (red) shown in  $\log_{10}(P1)$  vs.  $\log_{10}(S1)$  vs.  $\log_{10}(\text{Size})$  parameter space with  
5 classification accuracy of 99%. 2D projections of the data are shown at axes limits with smaller  
6 markers. (b) Concentration of aerosol particles, ice crystals, and water droplets as a function of  
7 chamber RH. Error bars represent classification uncertainty. (c) Fraction of particles activated as  
8 ice crystals and water droplets as a function of chamber RH. Error bars represent classification  
9 uncertainty.



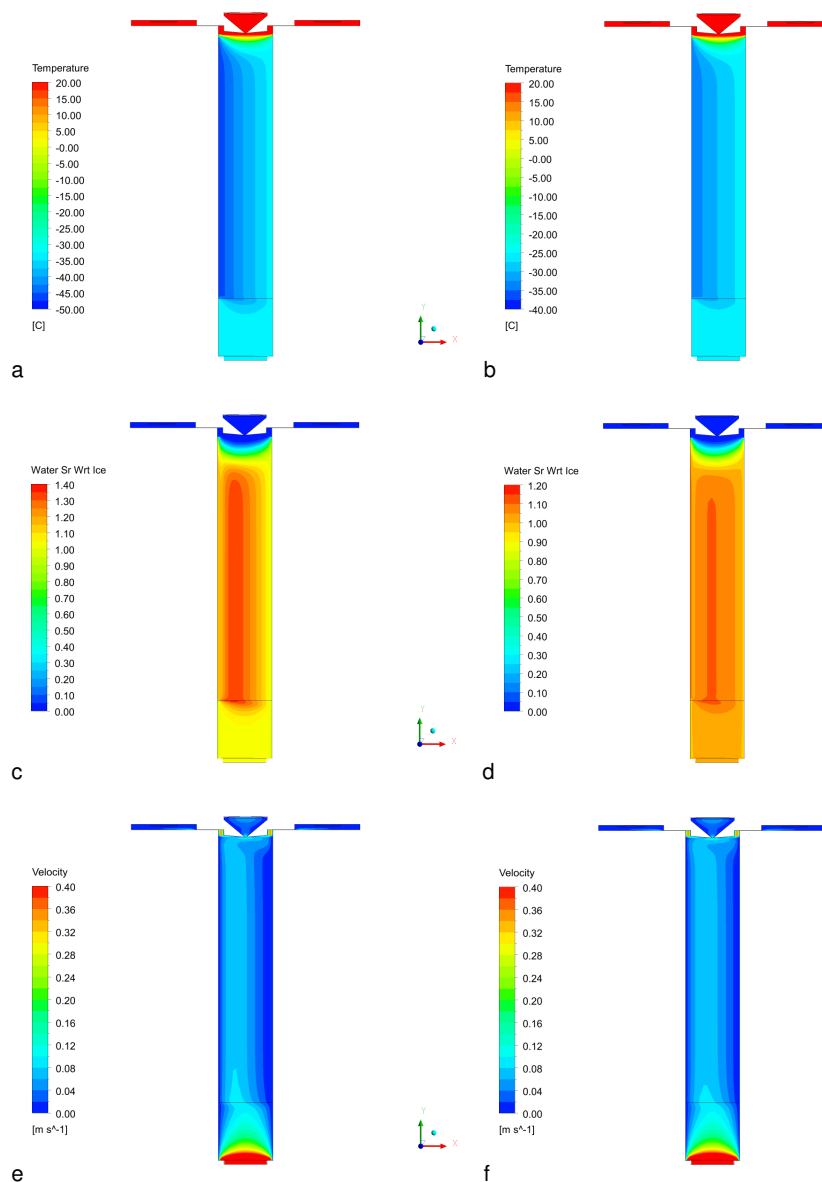
1  
2 Figure 8. Particle sizing and transmission efficiency of the SPIN detector. (a) Detector intensity  
3 counts versus test particle size before and after the freezing experiments in this study. Dashed  
4 line shows power law fit to the data. (b) Size-dependent counting efficiency of AS particles with  
5 sigmoid fit. Error bars show measurement uncertainty.



1  
2 Figure 9. Experimental homogeneous freezing results. The hatched and shaded area shows where  
3 homogeneous freezing is expected to occur (below  $-38^{\circ}\text{C}$  and above the Koop line (Koop et al.,  
4 2000)). The color contours show interpolated activated fraction of ice crystals as a function of  
5 chamber conditions from 38 experiments (white areas are where no data are present).



1  
2 Figure 10. Experimental heterogeneous ice nucleation results and comparison to literature with  
3 polydisperse NX illite, AgI, and 500nm kaolinite particles. AS droplet breakthrough data and  
4 corresponding droplet breakthrough (quadratic) fit line are shown in green. Error bars represent  
5 uncertainty in lamina temperature and SS conditions.



1

2 Figure 11. Fluent simulation results for two sets of chamber conditions in a cross-sectional view.

3 Left column shows results for nominal lamina temperature of  $-40^{\circ}\text{C}$  and lamina  $S_{\text{ice}}$  at 1.3. (a)

4 Temperature, (c)  $S_{\text{ice}}$ , and (e) flow velocity. Right column shows results for nominal lamina

5 temperature of  $-30^{\circ}\text{C}$  and lamina  $S_{\text{ice}}$  at 1.1. (b) Temperature, (d)  $S_{\text{ice}}$ , and (f) flow velocity.